Nanoscale

PAPER

View Article Online
View Journal | View Issue

Cite this: *Nanoscale*, 2017, **9**, 2020

MoO_{3-x} quantum dots for photoacoustic imaging guided photothermal/photodynamic cancer treatment†

Dandan Ding,‡[a,b] Wei Guo,‡[a,c] Chongshen Guo,*[a] Jianzhe Sun,[a,b] Nannan Zheng,[a,c] Fei Wang,[a,c] Mei Yan[a] and Shaoqin Liu*[a,c]

Received 21st November 2016,
Accepted 5th January 2017

DOI: 10.1039/c6nr09046j

rsc.li/nanoscale

A theranostic system of image-guided phototherapy is considered as a potential technique for cancer treatment because of the ability to integrate diagnostics and therapies together, thus enhancing accuracy and visualization during the treatment. In this work, we realized photoacoustic (PA) imaging-guided photothermal (PT)/photodynamic (PD) combined cancer treatment just *via* a single material, MoO_{3-x} quantum dots (QDs). Due to their strong NIR harvesting ability, MoO_{3-x} QDs can convert incident light into hyperthermia and sensitize the formation of singlet oxygen synchronously as evidenced by *in vitro* assay, hence, they can behave as both PT and PD agents effectively and act as a "dual-punch" to cancer cells. In a further study, elimination of solid tumors from HeLa-tumor bearing mice could be achieved in a MoO_{3-x} QD mediated phototherapeutic group without obvious lesions to the major organs. In addition, the desired PT effect also makes MoO_{3-x} QDs an exogenous PA contrast agent for *in vivo* live-imaging to depict tumors. Compared with previously reported theranostic systems that put several components into one system, our multifunctional agent of MoO_{3-x} QDs is exempt from unpredictable mutual interference between components and ease of leakage of virtual components from the composited system.

1. Introduction

Photodynamic therapy (PDT) and photothermal therapy (PTT) are two kinds of typical phototherapy strategies that have long been attracting considerable scientific attention.[1–3] With PDT, irreversible damage to malignant tumors is realized by reactive oxygen species (ROS) which are generated when the photosensitizer (PS) located at the tumor site is exposed to external incident light of a suitable wavelength *via* photochemical reactions to exhaust tissue oxygen.[4,5] PDT has been proven to be effective in its early stage of treatment as the ROS can be produced as soon as a laser is provided, but it suffers severely from therapeutic deterioration as the treatment time elapses owing to photodegradation of the PS and depletion of tissue oxygen, both of which result in a cease in ROS generation.[6] In addition, the maximal absorption band in the visible region[7] and the poor water-solubility[8] of most PSs also strongly limit PDT towards further clinical translation. Meanwhile, for PTT, a photothermal (PT) agent is employed for selective local heating of the diseased region to cure the abnormal cells or malignant tumors upon laser irradiation. Heat accumulation occurring in PTT becomes stronger with time and produces a hyperthermic effect which causes denaturation of proteins and disruption to the cytomembrane, thus leading to a destruction of diseased tissue eventually. Unlike PDT, PTT is applicable to hypoxic tissues; however, the vital drawback of PTT is that the hyperthermia can also cause a heat shock response, which weakens the treatment efficacy by suppressing apoptosis.[9] Obviously, PDT therapeutic efficiency decreases with increasing irradiation time, while the PTT efficiency increases with increasing irradiation time. Thus, some efforts have focused on the combination of early-stage effective PDT and late-stage effective PTT into a dual-therapy model, and created a synergistic effect with improved treatment outcome.[10–13] It is a pity that, owing to the mismatch of the optical absorption band between PT agents and PS agents, two individual lasers should be applied synchronously to the system so that the PTT and PDT can be excited separately.[14] This administration process is

[a]*Key Lab of Microsystem and Microstructure (Ministry of Education), Harbin Institute of Technology, Harbin 150080, China. E-mail: chongshenguo@hit.edu.cn*
[b]*School of Chemistry and Chemical Engineering, Harbin Institute of Technology, Harbin 150080, China*
[c]*School of Life and Technology, Harbin Institute of Technology, Harbin 150080, China*

† Electronic supplementary information (ESI) available: XPS and FT-IR spectra of MoO_{3-x}; calculation details of the photothermal conversion efficiency; MTT assay result; photoacoustic signal of the MoO_{3-x} solution; the *in vitro* phototherapeutic effect of the MoO_{3-x} QDs against HeLa cells. See DOI: 10.1039/c6nr09046j

‡ These authors contributed equally to this work.

complicated to operate and it is hard to focus two laser beams on the same site. Screening the PS agent to ensure that its absorption band coincides with that of the PT agent seems like an option to resolve this, in order to perform simultaneous PDT/PTT treatment upon single laser irradiation. Nevertheless, the photo-generated electrons or ROS in the PDT part being quenched by the plasmonic PT agent, together with thermal decomposition of the PS agent induced by PT nanostructures, resultantly weaken the role of PDT.[15] As a consequence, it is extremely urgent and of great significance to carry out the combined PDT/PTT dual-therapy model with a single material that behaves with the characteristics of both the PT and PS agents, which is expected to show a better therapeutic effect, free of mutual interferences, with simple operation and higher stability compared with the previously reported "put together multicomponent in one" strategy.[16–18]

Nowadays, theranostics has drawn particular attention because it combines cancer diagnosis and treatment, thus enhancing the visualization of the cancer therapy.[19–29] Photoacoustic imaging tomography (PAT) is a promising imaging modality relying on the measurement of ultrasonic waves that are produced by biological tissue or a PA contrast agent when the laser pulses treat them.[30,31] PAT often shows improved high resolution and contrast of 3D tissue images because it inherits the merits of high contrast from optical imaging and deep tissue penetration from ultrasonic imaging. Although a PA-imaging guided PDT/PTT theranostic system has been tentatively tried, the existing problems of current multi-functional cancer treatment systems are their complex composition,[32] unpredictable mutual interference between components[33] and ease of leakage of virtual components from the composited system.[34] To overcome these imperfections, we herein developed a multi-functional theranostic system just using a single material of MoO_{3-x} quantum dots (MoO_{3-x} QDs for short later), which can realize PA-imaging and dual-therapy (PDT/PTT) for cancer treatment *in vitro* and *in vivo*. The MoO_{3-x} QDs show strong optical absorption in the NIR range. Based on this unique property, the hyperthermic effect and singlet oxygen could be produced simultaneously by MoO_{3-x} QDs under laser irradiation for executing the dual-therapy of PDT/PTT. Their excellent photothermal conversion ability also makes MoO_{3-x} QDs a strong PA contrast agent.

2. Experimental

2.1 Synthesis of MoO_{3-x} QDs

Firstly, 0.5 g of molybdenum powder was dissolved into 7.5 ml of hydrogen peroxide (30%) to form a homogeneous solution. Then, the resulting solution was diluted into a 30 ml solution with deionized water. A platinum net was dipped into the above solution to decompose excess hydrogen peroxide. After that, 1 g of chitosan (M_w = 2000) was added to the resulting solution. Afterwards, the solution was transferred to a Teflon-lined autoclave of 100 mL internal volume, then underwent a hydrothermal reaction in an electric oven at 80 °C. After 24 h of reaction, the product was obtained *via* dialysis and a lyophilization process.

2.2 Characterization

Transmission electron microscopy (TEM) images were obtained using a microscope at an acceleration voltage of 200 kV (FEI Tecnai G2 F30). The crystal phase composition of the sample was determined by X-ray diffraction measurement (XRD, Shimadzu XD-D1) using graphite-monochromized CuK_α radiation. The Mo_{3d} binding energy of the sample was determined using X-ray photoelectron spectroscopy (XPS, Perkin Elmer PHI 5600). The optical properties were measured using a spectrophotometer (U-4100, Hitachi). NIR laser irradiation induced temperature elevation was recorded using a thermographic meter (FLIR System i7). MTT experiments were performed on a microplate reader (Infinite M200, Tecan).

2.3 Cell lines and cell culture

HeLa cells (cervical cancer cell line) and L02 cells (human hepatic cell line) were purchased from the cell bank of the Chinese Academy of Sciences, Shanghai, China. Cells were grown in a monolayer in RPMI-1640 with supplementation of 10% (v/v) fetal bovine serum (FBS, Clark, Australia Origin) and penicillin/streptomycin (100 U mL^{-1} and 100 mg mL^{-1}, Gibco) in a humidified 5% CO_2 atmosphere at 37 °C.

2.4 Cytotoxicity assay *in vitro*

The cytotoxicity of the MoO_{3-x} QDs was determined using a standard MTT assay. The assay was carried out in triplicate according to the following method. HeLa cells or L02 cells were seeded into 96-well plates at a density of 1×10^4 per well in 200 μL of media and were allowed to grow overnight. After that, the cells were incubated with different concentrations of MoO_{3-x} QDs for 24 h. Then, the cells were incubated in media containing 20 μL of MTT (5 mg mL^{-1}) for 4 h. The media containing MTT were removed, and 150 μL of DMSO was added to dissolve formazan crystals at room temperature for 30 min. Then, the optical absorbance was measured at 490 nm using a multi-detection microplate reader (SynergyTM HT, BioTek Instruments Inc., USA). The cellular metabolic activity was expressed as relative cellular viability, which is normalized with that of the untreated cell control.

2.5 Detection of ROS

For the extracellular ROS generation test, a 1,3-diphenylisobenzofuran (DPBF) probe was employed to detect the ROS production.[35] 20 μL of *N*,*N*-dimethylformamide solution containing DPBF (1 mg mL^{-1}) was added to 3 mL of pure water or MoO_{3-x} QD solution. Then, both of these solutions were left in the dark under magnetic stirring and then irradiated by a 880 nm NIR laser. After centrifugation, the optical absorbance of the supernatant at 410 nm was determined using a UV-Vis spectrophotometer. The degree of ROS production is reflected by the reduction in the value of the absorbance at 410 nm. Intracellular ROS generation was examined using a H_2DCFDA probe.[34] 5×10^3 cells were seeded into a 6-well plate and

incubated at 37 °C in a humidified atmosphere with 5% CO_2 for 24 h. Afterwards, HeLa cells were incubated with 200 μL of MoO_{3-x} QDs (250 μg mL^{-1}) at 37 °C for 24 h. The positive control cells were cultivated with 200 μL of 50 mM H_2O_2 at 37 °C for 30 min. Then, all of the cells were stained with 50 μL of H_2DCFDA (10 mM in DMSO) for 1 h at 37 °C. Thereafter, the cells were washed with PBS and irradiated under a 2 W cm^{-2} 880 nm laser for 10 min. Fluorescence images were immediately measured using an Olympus BX53 fluorescence microscope (Olympus, Tokyo, Japan) using an excitation wavelength of 488 nm and an emission wavelength of 515–540 nm.

2.6 *In vitro* and *in vivo* PA imaging

Detection of the PA imaging signals was performed using a MOST Invision 128 system. For the *in vitro* test, 1 mL of MoO_{3-x} QD aqueous dispersion at various concentrations (0, 31.25, 62.5, 125, 250 and 500 ppm) was added into an agar-phantom container and placed in the testing system for signal detection. The *in vivo* PA imaging was investigated on HeLa tumor-bearing mice. The PA signals from the tumor site were collected before and after intratumoral or tail intravenous injection of MoO_{3-x} solution (100 μL, 2 mg mL^{-1}).

2.7 *In vitro* photoablation of cancer cells

HeLa cells were seeded in a 35 mm tissue culture dish at a density of 3×10^5 cells per dish and allowed to grow for 24 h at 37 °C until they were nearly confluent. Then, the culture medium was replaced with 2.0 mL of medium containing 0.25 mg mL^{-1} MoO_{3-x} QDs. The cells were further incubated for 24 h, and then rinsed three times with PBS to remove the nonspecifically adsorbed nanoparticles. Then, the cells were irradiated by a 880 nm laser for different time intervals (4, 6, and 10 min) at a powder density of 2 W cm^{-2}. The irradiated cells were stained with Calcein-AM and PI to distinguish the living and dead cells, respectively. The stained cells were then examined using an Olympus BX53 fluorescence microscope.

2.8 *In vivo* photoablation studies

Female BALB/c nude mice (5 weeks, 18–22 g) were obtained from Vital River Experimental Animal Technical Co., Ltd. (Beijing) and all of the *in vivo* experiments were implemented according to the criteria of the National Regulation of China for Care and Use of Laboratory Animals. Firstly, the tumors were inoculated by subcutaneous injection of 1×10^7 HeLa cells in the left flank of each BALB/c mouse using 50% Matrigel. When the tumor size reached about 200 mm^3, the tumor-bearing nude mice were randomized into five groups (n = 5 for each group) and 100 μL of PBS or MoO_{3-x} QD (1 mg mL^{-1}) solution was intratumorally injected into the mice: the control group (1) received PBS injection only; group (2) received MoO_{3-x} QD injection only; group (3) received 880 nm laser irradiation for 10 min; group (4) received MoO_{3-x} QD injection and 880 nm laser irradiation for 5 min; group (5) received MoO_{3-x} QD injection and 880 nm laser irradiation for 10 min. The power density of the NIR laser was 2 W cm^{-2} and the treatment began 2 hours post-intratumoral injection. The therapeutic effectiveness for each group was evaluated by measuring the tumor volume, which is calculated as V = length × width^2. The relative tumor volume was calculated as V/V_0, where V_0 is the initial tumor volume prior to treatment. The relative body weight was calculated as W/W_0, where W_0 is the initial body weight prior to treatment.

2.9 Histology analysis

Histology analysis was carried out after treatment by sacrificing the mice. The tumors and major organs including the liver, kidney, heart, lung and spleen from the control and treated groups were isolated. Then, the tumors and organs were fixed in 4% paraformaldehyde solution and embedded in paraffin. The sliced tumor tissues and organs were stained with Hematoxylin and Eosin (H&E), and then examined using an Olympus BX53 fluorescence microscope (Olympus, Tokyo, Japan).

3. Results and discussion

3.1 Synthesis and characterization of MoO_{3-x} QDs

In this work, MoO_{3-x} QDs were fabricated *via* a hydrothermal method in which metallic Mo was used as the Mo source and chitosan functioned as both the capping agent and reducing agent at 80 °C for 24 h. The TEM observation in Fig. 1a clearly shows that the obtained sample is composed of many homogeneously dispersed tiny dots, and the particle size is around 2.5 nm. Such a small size of dot is expected to be able to escape from the capture of the reticuloendothelial system, resulting in optimal drug administration at the tumor site. Furthermore, the HR-TEM image shown in Fig. 1b presents two selected typical nanodots, both of which depict clear

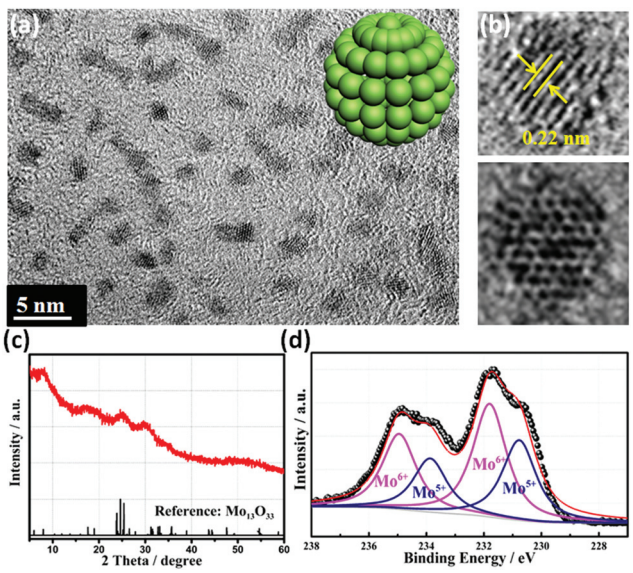

Fig. 1 (a) TEM image, (b) HR-TEM image, (c) XRD pattern and (d) Mo 3d XPS spectra of MoO_{3-x} QDs. (Inset of (a) shows a schematic of a quantum dot.)

lattice fringes, indicating a definite crystalline nature. The crystalline lattice constant of one nanodot is determined to be 0.22 nm. Then, the phase and crystalline nature of the MoO_{3-x} QDs were further explored by XRD analysis (Fig. 1c). Owing to the confined dimensions, the XRD diffractive intensity of the MoO_{3-x} QDs is too weak to be straightforwardly ascribed to a Mo species exactly; nevertheless, it is closer to the reduced species of $Mo_{13}O_{33}$. The composition and oxidation state were checked using X-ray photoelectron spectroscopy (XPS) next. In the full range of the XPS spectra, the peaks corresponding to the elements N, C, Mo and O are discerned (Fig. S1†). The presence of N and C may originate from the chitosan decoration. For a more detailed Mo 3d spectrum, the overall curve could be fitted into two groups of spin–orbit doublets, attributed to two different oxidation states of Mo ions. The first doublets located at 234.9 and 231.8 eV could be assigned to Mo^{6+} ions, while the second doublets with relatively lower binding energies of 233.9 and 230.8 eV result from Mo atoms in the +5 oxidation state[36] (Fig. 1d). The evidence of mixed valent Mo ions strongly supports the reduced nature of MoO_{3-x}. This is as we expected; that is, chitosan can act as a reducing agent to convert part of Mo^{6+} into Mo^{5+} under our hydrothermal conditions. Another initial assumption is that chitosan can also behave as a capping agent, which is proven by the FT-IR result shown in Fig. S2.† For the sample of MoO_{3-x} QDs, the peaks at 1149 and 1076 cm^{-1} are related to the C–O stretching vibration mode from the C–OH part, while the peak at 764 cm^{-1} belongs to the C–H bending vibration, all of which are consistent with the control of chitosan. Usually, typical Mo═O stretching frequencies at 991 and 960 cm^{-1} can be identified for molybdenum oxide species or polymolybdates, and one additional characteristic Mo–O–Mo vibration for α-MoO_3.[37] In this work, the MoO_{3-x} quantum dots showed an obvious shift to 973 and 911 cm^{-1}, which is due to the formation of the Mo–O–C bond mode, thus confirming that there is a strong interaction between chitosan and the MoO_{3-x} surface by chemical bonding. On the merit of this, chitosan-coated MoO_{3-x} QDs show good biocompatibility. As shown in Fig. S3,† the MTT assay results reveal that there is no significant cytotoxicity of the MoO_{3-x} QDs for carcinoma HeLa cells and normal L02 cells at concentrations below 0.5 mg mL^{-1}. Even after 24 h of incubation with 0.5 mg mL^{-1} MoO_{3-x} QDs, the L02 and HeLa cells still kept over 90% of their metabolic activity.

3.2 Photoabsorption and photothermal effect of MoO_{3-x} QDs

Optical absorption in the NIR area and consequent photothermal conversion are prerequisites for the targeted photothermal therapy. Hence, we firstly investigated the optical properties of the MoO_{3-x} QD powder. As shown in Fig. 2a, the powder sample of the MoO_{3-x} QDs exhibits high optical absorbance in the whole biological window of 700–1300 nm, which is due to the free electron induced LSPR effect.[38,39] In addition, the MoO_{3-x} QD dispersed solution also demonstrated obvious photoabsorption which enhanced remarkably along with a concentration increment, especially in the NIR part as expected

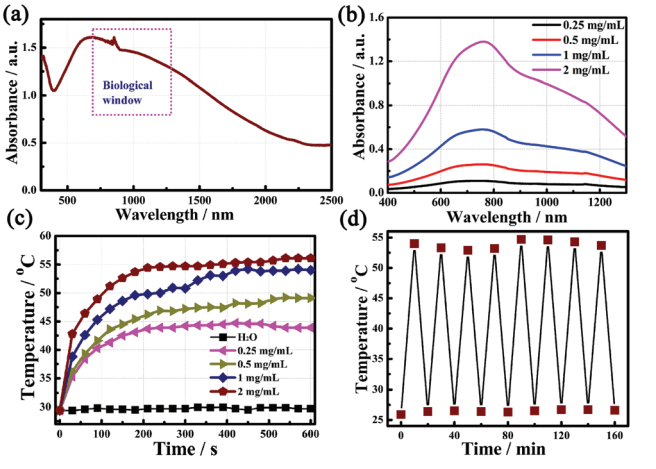

Fig. 2 (a) Powder absorbance of MoO_{3-x} QDs; (b) UV-Vis-NIR absorption spectra of solutions containing varied amounts of MoO_{3-x} QDs; (c) NIR irradiation induced temperature elevation of MoO_{3-x} QD aqueous solution with different concentrations, and that of water, which was used as the control (NIR 880 nm, power density: 2 W cm^{-2}); (d) cycling stability test of the photothermal conversion after 8 cycles.

(Fig. 2b). Given the satisfying absorption in the NIR region, we next evaluated the photothermal conversion properties by measuring the thermal variations of the MoO_{3-x} QD aqueous suspensions under 880 nm NIR laser irradiation with a power density of 2 W cm^{-2} in real-time *via* a thermographic camera. As shown in Fig. 2c, the control of pure water shows a negligible temperature rise upon laser irradiation. In sharp contrast, all of the MoO_{3-x} QD dispersions exhibited remarkable temperature elevation over time, suggesting that the MoO_{3-x} QDs could rapidly and efficiently convert the NIR photoenergy into local hyperthermia under irradiation. Additionally, a dose-dependent photothermal effect further demonstrates the role of MoO_{3-x} as an excellent PT agent to cause hyperthermia, rather than the absorption of light by water. Next, we have also examined the cycling stability of the photothermal test. The MoO_{3-x} QD solution was exposed to NIR irradiation for 10 min and then naturally cooled for another 10 min for each cycle. After eight cycles, there is a negligible change in the temperature rising behavior, confirming the good photostability of the MoO_{3-x} QDs. Finally, quantitative confirmation of the photothermal conversion efficiency was performed according to the literature method.[40] By measuring the temperature rise under laser irradiation and the natural cooling curves of 0.45 ml (1 mg mL^{-1}) of MoO_{3-x} solution, the 880 nm laser induced photothermal conversion efficiency (η) was calculated to be 25.5%. (For the more detailed calculation process of η, please see Fig. S4 & 5 in the ESI.†) The strong optical absorbance in the NIR region and high photothermal conversion ability suggest that MoO_{3-x} QDs can be excellent agents for PA and PT.

In addition, we also checked the chemical stability of the MoO_{3-x} QDs by laser irradiation heating both *in vitro* and *in vivo*. For the *in vitro* group, the MoO_{3-x} QDs after 8 cycles of

the photothermal conversion test (shown in Fig. 2d) were collected. As for the *in vivo* group, 0.5 ml (2 mg ml^{-1}) of MoO_{3-x} QD solution was intratumorally injected into the tumor site of the tumor-bearing nude mice. After 10 min of laser irradiation, the MoO_{3-x} QDs were collected from the tumor site by dissection. Then, XPS measurement was used to investigate the chemical valence changes of the sample after the treatments. As shown in Fig. S6,† there is a negligible change in the relative intensity between Mo^{5+} and Mo^{6+} for the sample after either *in vitro* or *in vivo* treatment, illustrating acceptable chemical stability of the MoO_{3-x} QDs under NIR laser irradiation and the feasibility of further applying MoO_{3-x} QDs to phototherapy.

3.3 Singlet oxygen generated by MoO_{3-x} QDs

The production of cytotoxic ROS surrounding the tumor cells is the principle for PDT implementation. To verify the capability of the MoO_{3-x} QDs to sensitize formation of ROS upon photoexcitation, a 1,3-diphenylisobenzofuran (DPBF) probe was firstly employed to detect the ROS production.[35] The DPBF probe is a substance with a characteristic absorption peak at 410 nm. Once it meets singlet oxygen, $^1O_2$, DPBF will be decomposed to produce 1,2-dibenzoylbenzene, thus leading to a decrement in the optical absorption value at 410 nm. Because of this, a spectroscopic method could be used to evaluate the degree of $^1O_2$ production.[41] As displayed in Fig. 3a, compared with the control test of pure water, the optical absorption values of the MoO_{3-x} QD dispersed DPBF solution significantly decreased under 880 nm irradiation over time, illustrating an excellent photosensitive ability of MoO_{3-x} QDs to produce singlet oxygen. Next, the intracellular generation of ROS in HeLa cells induced by MoO_{3-x} QDs upon NIR light irradiation was investigated (Fig. 3b–f) further. The HeLa cells treated with H_2O_2 (50 mM) were used as a positive control (Fig. 3f). Visualization of the intracellular generation of singlet oxygen was realized by a probe of 2′,7′-dichlorofluorescin diacetate (H_2DCFDA), which is a cell-permeable non-fluorescent probe. However, it can convert to highly fluorescent 2′,7′-dichloroflorescein with a green color after oxidation by singlet oxygen. As displayed in Fig. 3e & f, strong green fluorescence is observed in the H_2O_2 positive control and the group of MoO_{3-x} QDs in combination with NIR irradiation. This is in marked contrast to there being almost no discriminable fluorescence for the negative control group and very weak fluorescence signals for the only NIR light irradiation group, thereby suggesting that NIR light triggered MoO_{3-x} QDs can produce sufficient ROS in the cells and are an eligible candidate for further PDT.

3.4 *In vitro* and *in vivo* PA imaging

Photoacoustic imaging tomography (PAT), which is a burgeoning noninvasive imaging modality, has received wide attention in recent years.[20] Photoacoustic imaging relies on the detection of thermoelastic expansion and consequent wideband

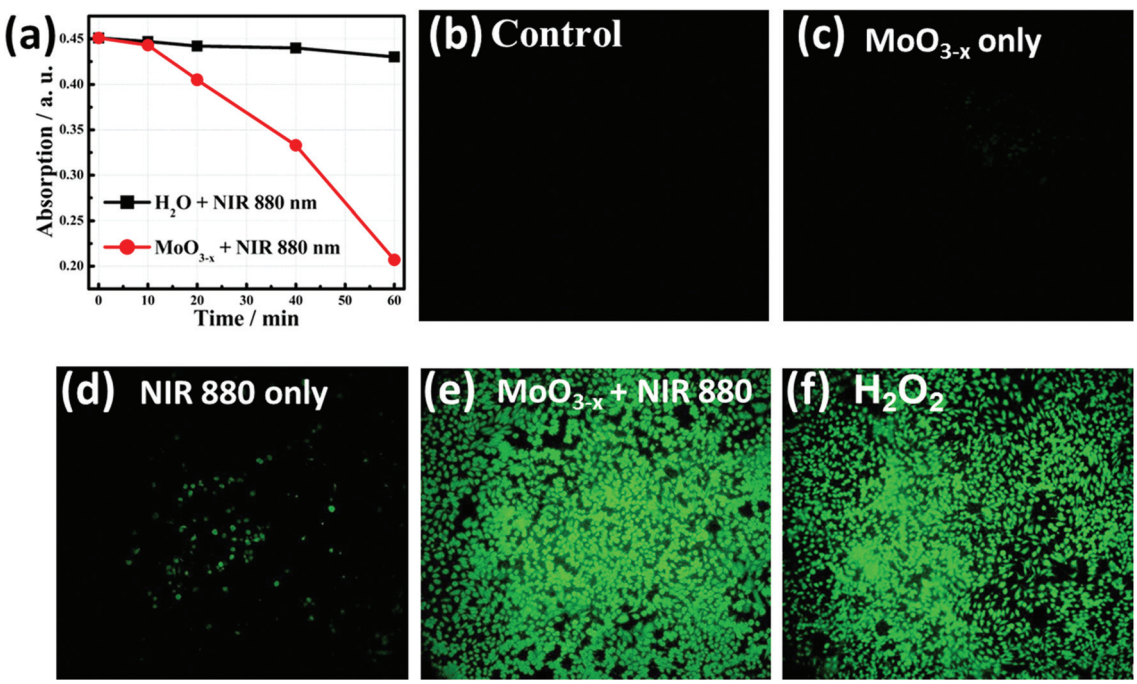

Fig. 3 Detection of singlet oxygen generation by NIR light triggered MoO_{3-x} QDs. (a) Absorption value of the MoO_{3-x} QD solution after addition of the DPBF probe under different irradiation times. Fluorescence microscope images of ROS generation in HeLa cells that received different treatments: (b) control group without any treatment, (c) cells treated with MoO_{3-x} QDs only, (d) cells irradiated by NIR light of 880 nm only, (e) cells treated with NIR light of 880 nm and MoO_{3-x} QDs, and (f) H_2O_2 as a positive control. (NIR laser: 2 W cm^{-2}, 10 min. Green: ROS indicator H_2DCFDA. Scale bar: 200 μm).

ultrasonic emission induced by tissue absorption of light. However, many pathological tissues are not endogenous PA contrast agents owing to their limited photoabsorption. Thus, exogenous light-absorbers are highly needed for PA imaging.[42] Considering the excellent photothermal effect of MoO_{3-x} QDs, they appear to be an ideal PA contrast agent. As might be expected, the photoacoustic signal of the MoO_{3-x} QD dispersion remarkably enhanced as a function of concentration in the *in vitro* experiment (Fig. 4a), and a good linear relationship between the dose of MoO_{3-x} QDs and the PA signals at 880 nm was found (Fig. S7†). Encouraged by the above positive results, the MoO_{3-x} QDs were further utilized as a PA contrast agent for *in vivo* tumor imaging. The HeLa tumor-bearing mice were injected with 100 μL of MoO_{3-x} QDs (2 mg mL^{-1}) *via* either intratumoral injection or tail intravenous injection. The PA signal from the tumor site of the mice was collected at different time intervals post injection. For the intratumoral injection group, the PA signal was enhanced remarkably by the MoO_{3-x} QDs and the tumor site was clearly discriminated during the whole observation stage of 24 h, suggesting a long-acting tumor accumulation of MoO_{3-x} QDs *via* intratumoral administration (Fig. 4b). Meanwhile, for the tail intravenous injection group, the strongest PA signal occurred at 4 h post injection and thereafter the intensity became weaker and weaker (Fig. 4c & S8†). After 12 h, the PA signal from the tumor site is not notable. The passive tumor accumulation at the initial phase of 4–6 h after intravenous injection of MoO_{3-x} QDs may be due to the enhanced permeability and retention effect (EPR) of tumor tissues, especially for such small quantum dots. However, it suffers from short retention time as compared with that of the intratumoral injection group. Even so, the above results still suggest that MoO_{3-x} QDs can behave as a promising PA contrast agent for tumor imaging *via* either intratumoral or intravenous injection.

3.5 Phototherapeutic studies *in vitro* and *in vivo*

Encouraged by the desirable photothermal effect and photodynamic ROS generation, we next surveyed the phototherapeutic effect of MoO_{3-x} QDs in killing HeLa cancer cells under NIR light irradiation by fluorescent visualization of photoablation induced live-dead assay. HeLa cells were incubated with MoO_{3-x} QDs for 24 h and then irradiated by an 880 nm laser for varied durations. After exposure to laser treatment, Calcein AM with green fluorescent labeling and propidium (PI) with red fluorescent labeling were used to distinguish the living and dead HeLa cells, respectively. As can be seen in Fig. 5a–c, the control group of cells treated with MoO_{3-x} QDs alone or the laser only irradiation group showed remarkable green fluorescence but no red fluorescence, indicating that either MoO_{3-x} QDs or NIR alone caused nearly no cancer cell death. In contrast, the cells treated with MoO_{3-x} QDs and NIR 880 nm laser irradiation together induced obvious enhanced cell death as evidenced by the striking red fluorescence from the irradiated region, and the area of the dead cell circle enlarged dramatically with prolonged irradiation duration. Furthermore, photodestruction of HeLa cells also can be enhanced by increasing the laser power density and concentration of the MoO_{3-x} QDs provided, (Fig. S9 & 10†), both of which also contribute to a higher temperature increment and more ROS generation. Thus, *in vitro* photodestruction of cancer cells could be explained by heat diffusion and reactive oxygen species (ROS) migration induced lysosome damage and cytoskeleton protein degradation, which have been proven in our previous work.[43]

Next, we employed MoO_{3-x} QDs for further *in vivo* cancer treatment. HeLa tumor-bearing nude mice were intratumorally injected with 100 μL of PBS for the control group and MoO_{3-x} QDs (1 mg mL^{-1}) for the treatment group. The tumor-bearing nude mice were then irradiated by a NIR laser of 2 W cm^{-2}

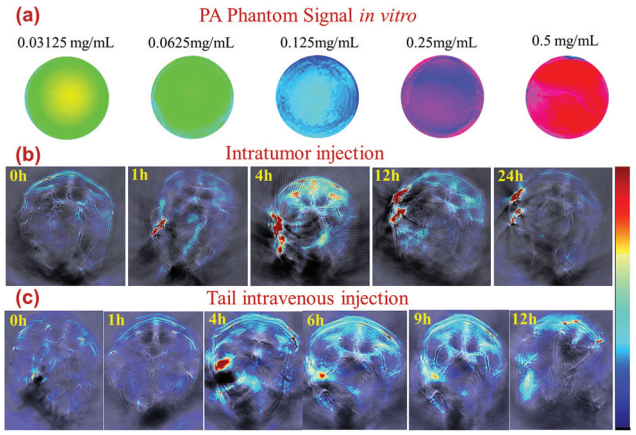

Fig. 4 PA imaging *in vitro* and *in vivo*. (a) PA phantom images *versus* MoO_{3-x} QD concentrations. *In vivo* PA images of HeLa tumor-bearing mice before and after injection of MoO_{3-x} QDs for different times. (b) MoO_{3-x} QDs were administered *via* intratumoral injection. (c) MoO_{3-x} QDs were administered *via* tail intravenous injection.

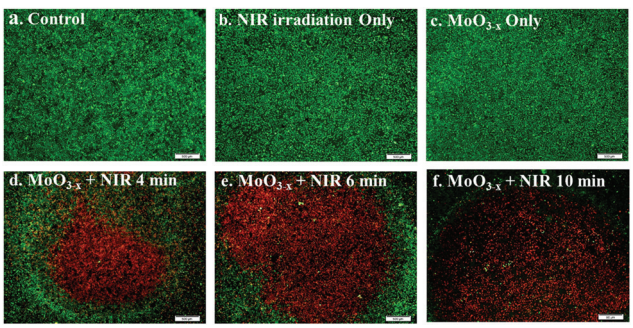

Fig. 5 *In vitro* phototherapeutic effect of MoO_{3-x} QDs against HeLa cells. Fluorescence images and dead cell circle area of HeLa cells after different treatments. (a) HeLa cell control, (b) HeLa cells treated with 2 W cm^{-2} NIR 880 nm laser irradiation for 10 min, (c) HeLa cells incubated with 0.25 mg mL^{-1} MoO_{3-x} QDs for 24 h, (d–f) HeLa cells treated with MoO_{3-x} QDs and different durations of 880 nm laser irradiation (scale bar: 500 μm). Images were taken 24 h post NIR irradiation *via* a live-dead assay using Calcein AM (live cells, green fluorescence) and propidum iodide (PI) (dead cells, red fluorescence).

and the body surface temperature of the tumor site was monitored using an IR thermal camera after exposure to the NIR laser. As depicted in Fig. 6A, for the control group of mice injected with PBS, the surface temperature of the tumor increased slightly within 10 min under 880 nm irradiation, which may be related to the minimal photoabsorption of 880 nm laser light from hemoglobin. In comparison, the tumor temperature of the MoO_{3-x} QD mediated group can reach up to 51 °C under irradiation, which is sufficient for cancer cell death. Cancer cells are less tolerant to hyperthermia than normal cells and even short exposure (4–6 min) to a temperature higher than 48 °C would result in irreversible damage.[44] Then, the *in vivo* phototherapeutic effects of the MoO_{3-x} QDs were evaluated. The tumor-bearing nude mice were randomized into five groups when the tumor size reached about 200 mm^3, (n = 5 for each group): control group (1) received PBS injection; group (2) received MoO_{3-x} QD injection; group (3) received 10 min laser irradiation; group (4) received MoO_{3-x} QD injection and 5 min laser irradiation; group (5) received MoO_{3-x} QD injection and 10 min laser irradiation. During the test, the tumor volume change and body weight were quantitatively monitored over time. As can be seen in Fig. 6B & C, the groups that received only MoO_{3-x} QD injection or only laser irradiation failed to depress the tumor development, indicating that neither the material itself nor the laser could effectively inhibit the tumor growth. The phototherapeutic groups that received both MoO_{3-x} QD injection and laser irradiation were investigated under two different therapeutic durations. It seems to be effective at an early stage for the MoO_{3-x} QD-mediated group receiving 5 min laser irradiation, but recurrence of tumor growth happened after the first week, indicating that short-term phototherapy is not sufficiently powerful for irreversibly damaging the tumor. Note that when the therapeutic time was extended to 10 min, it led to remarkable tumor suppression and the tumors of some mice were even ablated thoroughly after the treatment. In addition, as shown in Fig. 6D, the body weights of the mice in all of the groups showed no obvious losses, implying that the proposed method in this work has no acute toxicity. Therefore, we may arrive at the conclusion that the MoO_{3-x} QD mediated phototherapy can effectively inhibit tumor growth when the phototherapeutic time is over 10 min.

After the phototherapy, the tumor tissues and major organs including the liver, kidney, heart, lung and spleen were collected, fixed and sectioned for the Hematoxylin and Eosin (H&E) staining analysis to elucidate a possible mechanism for the tumor growth inhibition and animal systematic toxicity. As shown in Fig. 7, severe cellular necrosis and apoptosis were observed in the tumors that were treated by a combination of quantum dots and laser irradiation, in particular for the group with a longer therapeutic duration, implying that the synergistic effect of hyperthermia and ROS generation inducing cellular necrosis was the major cause for tumor growth inhibition. Meanwhile, the potential *in vivo* toxicity of MoO_{3-x} QDs to the major organs was studied *via* histological analysis and indicated no detectable lesions, such as necrosis, hydropic degeneration, inflammation or pulmonary fibrosis in the sections of tissues, suggesting that our MoO_{3-x} QDs are of satisfactory biosafety for *in vivo* cancer treatment (Fig. 8).

Finally, we investigated the metabolic pathway of the MoO_{3-x} QDs *via* measuring the Mo element distribution in the major organs using the ICP-MS method. For this purpose, HeLa-tumor-bearing nude mice were intravenously injected with 100 μL (1 mg mL^{-1}) of MoO_{3-x} solutions. Then, the organs were extracted at different time intervals post injection. At each interval, three mice were sacrificed to give an average

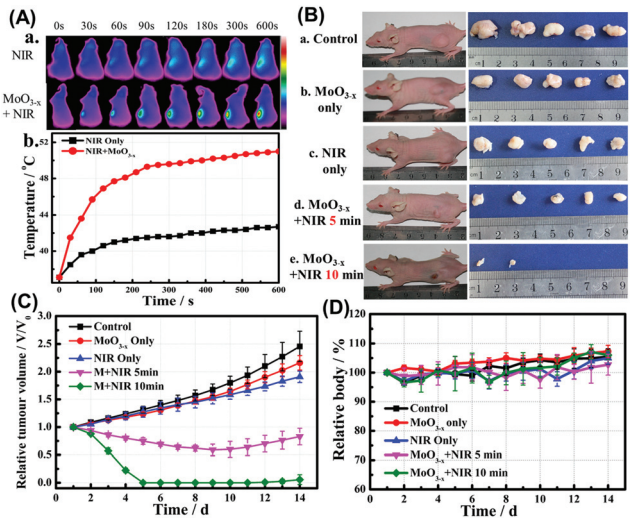

Fig. 6 *In vivo* phototherapeutic effect of MoO_{3-x} QDs. (A) a. Thermographic image of HeLa tumor-bearing mice injected with MoO_{3-x} QDs or PBS under 880 nm NIR laser irradiation. b. Temperature variation of tumors monitored using an IR thermal camera during laser irradiation. (B) Representative photos of the mice and tumors under various treatments after 14 days. (C) Quantitative measurement of the tumor volume in mice after various treatments. (D) Body weight of mice after various treatments.

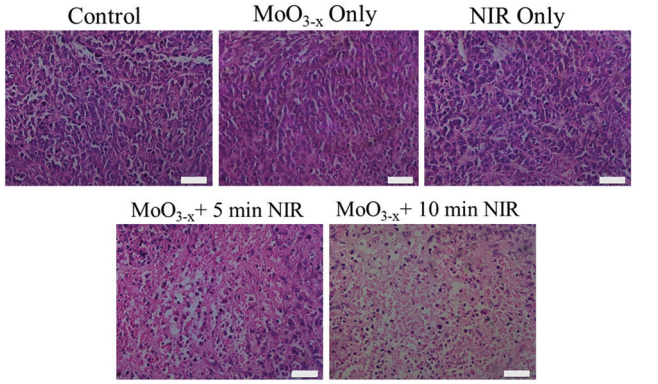

Fig. 7 Histology staining of tumor slices collected from different groups of mice after 14 days of treatment (red: necrocytosis; blue: apoptosis; scale bar: 50 μm).

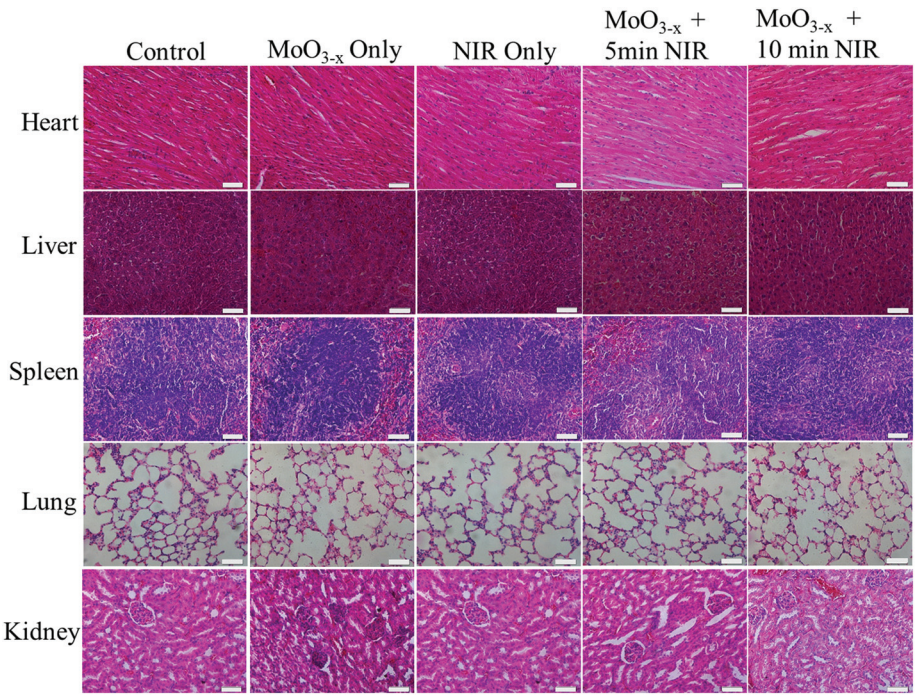

Fig. 8 Histology staining of major organs collected from different groups of mice after 14 days of treatment (scale bar: 50 μm).

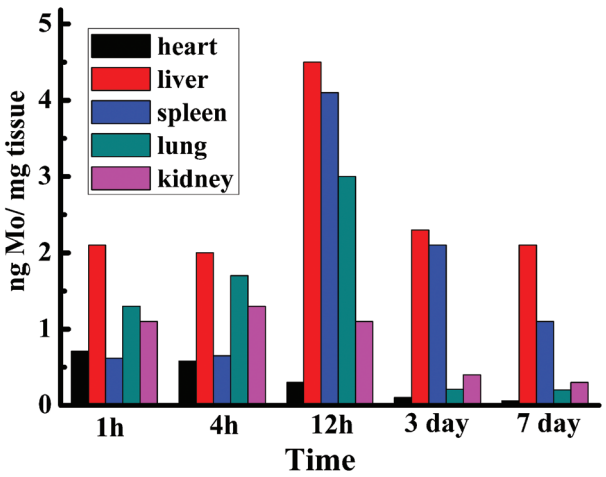

Fig. 9 The distribution of Mo element in mice organs.

value for the final result. As shown in Fig. 9, the overall level of Mo element in the organs increased in the first 12 h post injection, and thereafter the Mo content decreased with time. By comparison, a relatively higher quantity of Mo element accumulated in the liver and spleen during the whole stage, suggesting that MoO_{3-x} QDs could be metabolized by the liver and spleen to a greater extent, and slightly metabolized by other organs. The liver has been reported as the common clearance pathway because of Kupffer cells, which locate inside fenestrated sinusoids of liver blood vessels, and it can catch and destroy foreign nanomaterials. In addition, macrophages in the reticular meshwork of the spleen can also behave as a bio-filter to remove MoO_{3-x} QDs.[45]

4. Conclusions

In summary, we have fabricated a multifunctional theranostic agent of MoO_{3-x} QDs, which possesses PT, PD and PA multi-effects under NIR 880 nm irradiation. Thus, a PA-imaging guided PT/PD dual-therapy for cancer was realized. MoO_{3-x} QDs exhibited strong optical absorption in the biological window and a high photothermal conversion efficiency of 25.5% under 880 nm laser irradiation. Benefiting from this, MoO_{3-x} QDs produced local hyperthermia upon irradiation *in vitro* or at the tumor site *in vivo*, thus realizing the PT treatment outcome. Meanwhile, a non-fluorescent probe result revealed that NIR light triggered MoO_{3-x} resulted in an intracellular generation of singlet oxygen, producing PD efficacy. A living imaging study illustrated that MoO_{3-x} QDs could be employed as a PA contrast agent *via* either intratumoral or intravenous injection. Note that the MoO_{3-x} QDs showed a negligible cytotoxic effect in the dark, but remarkable cytotoxicity towards cancer cells under NIR laser irradiation *in vitro*. What is more, efficient tumor ablation *in vivo* can also be realized *via* local administration of MoO_{3-x} QDs to a tumor under laser irradiation after 14 days of treatment. According to the histological examination, the MoO_{3-x} QDs showed no apparent toxicity to the major organs of treated mice. Considering all of the above, MoO_{3-x} QDs will pave the way to use a single material for multifunctional theranostics.

Acknowledgements

This work was supported by the National Natural Science Foundation of China (51572059, 21303033, 81373359).

Notes and references

1 P. Vijayaraghavan, C. H. Liu, R. Vankayala, C. S. Chiang and K. C. Hwang, *Adv. Mater.*, 2014, **26**, 6689.
2 S. Lal, S. E. Clare and N. J. Halas, *Acc. Chem. Res.*, 2008, **41**, 1842.
3 R. Bardhan, S. Lal, A. Joshi and N. J. Halas, *Acc. Chem. Res.*, 2011, **44**, 936.
4 W. Guo, C. S. Guo, N. N. Zheng, T. D. Sun and S. Q. Liu, *Adv. Mater.*, DOI: 10.1002/adma.201604157; M. Yan, G. L. Li, C. S. Guo, W. Guo, D. D. Ding, S. H. Zhang and S. Q. Liu, *Nanoscale*, 2016, **8**, 17828; G. L. Li, C. S. Guo, M. Yan and S. Q. Liu, *Appl. Catal., B*, 2016, **183**, 142.
5 W. S. Kuo, Y. T. Chang, K. C. Cho, K. C. Chiu, C. H. Lien, C. S. Yeh and S. J. Chen, *Biomaterials*, 2012, **33**, 3270; V. Saxena, M. Sadoqi and J. Shao, *J. Pharm. Sci.*, 2003, **92**, 2090.
6 S. J. Wang, P. Huang, L. M. Nie, R. J. Xing, D. B. Liu, Z. Wang, J. Lin, S. H. Chen, G. Niu, G. M. Lu and X. Y. Chen, *Adv. Mater.*, 2013, **25**, 3055.
7 J. F. Lovell, C. S. Jin, E. Huynh, T. D. MacDonald, W. G. Cao and G. Zheng, *Angew. Chem., Int. Ed.*, 2012, **51**, 2429.
8 P. Huang, C. Xu, J. Lin, C. Wang, X. S. Wang, C. L. Zhang, X. J. Zhou, S. W. Guo and D. X. Cui, *Theranostics*, 2011, **1**, 240.
9 B. K. Wang, X. F. Yu, J. H. Wang, Z. B. Li, P. H. Li, H. Wang, L. Song, P. K. Chu and C. Li, *Biomaterials*, 2016, **78**, 27.
10 B. Jang, J. Y. Park, C. H. Tung, I. H. Kim and Y. Choi, *ACS Nano*, 2011, **5**, 1086.
11 J. Wang, G. Z. Zhu, M. X. You, E. Q. Song, M. I. Shukoor, K. J. Zhang, M. B. Altman, Y. Chen, Z. Zhu, C. Z. Huang and W. H. Tan, *ACS Nano*, 2012, **6**, 5070.
12 L. Gao, J. B. Fei, J. Zhao, H. Li, Y. Cui and J. B. Li, *ACS Nano*, 2012, **6**, 8030.
13 J. Lin, S. J. Wang, P. Huang, Z. Wang, S. H. Chen, G. Niu, W. W. Li, J. He, D. X. Cui, G. M. Lu, X. Y. Chen and Z. H. Nie, *ACS Nano*, 2013, **7**, 5320.
14 A. Sahu, W. I. Choi, J. H. Lee and G. Tae, *Biomaterials*, 2013, **34**, 6239.
15 J. Y. Kim, W. I. Choi, M. Kim and G. Tae, *J. Controlled Release*, 2013, **171**, 113.
16 R. Vankayala, C. L. Kuo, A. Sagadevan, P. H. Chen, C. S. Chiang and K. C. Hwang, *J. Mater. Chem. B*, 2013, **1**, 4379.
17 R. Vankayala, A. Sagadevan, P. Vijayaraghavan, C. L. Kuo and K. C. Hwang, *Angew. Chem., Int. Ed.*, 2011, **50**, 10640.
18 G. Pasparakis, *Small*, 2013, **9**, 4130.
19 D. D. Wang, Z. Guo, J. J. Zhou, J. Chen, G. Z. Zhao, R. H. Chen, M. N. He, Z. B. Liu, H. B. Wang and Q. W. Chen, *Small*, 2015, **11**, 5956.
20 H. Gong, Z. L. Dong, Y. M. Liu, S. N. Yin, L. Cheng, W. Y. Xi, J. Xiang, K. Liu, Y. G. Li and Z. Liu, *Adv. Funct. Mater.*, 2014, **24**, 6492.
21 L. S. Lin, Z. X. Cong, J. B. Cao, K. M. Ke, Q. L. Peng, J. H. Gao, H. H. Yang, G. Liu and X. Y. Chen, *ACS Nano*, 2014, **8**, 3876.
22 X. L. Sun, X. L. Huang, X. F. Yan, Y. Wang, J. X. Guo, O. Jacobson, D. B. Liu, L. P. Szajek, W. L. Zhu, G. Niu, D. O. Kiesewetter, S. H. Sun and X. Y. Chen, *ACS Nano*, 2014, **8**, 8438.
23 M. Zhou, R. Zhang, M. A. Huang, W. Lu, S. L. Song, M. P. Melancon, M. Tian, D. Liang and C. A. Li, *J. Am. Chem. Soc.*, 2010, **132**, 15351.
24 Y. K. Kim, H. K. Na, S. Kim, H. Jang, S. J. Chang and D. H. Min, *Small*, 2015, **11**, 2527.
25 X. J. Wang, C. Wang, L. Cheng, S. T. Lee and Z. Liu, *J. Am. Chem. Soc.*, 2012, **134**, 7414.
26 X. G. Ding, C. H. Liow, M. X. Zhang, R. J. Huang, C. Y. Li, H. Shen, M. Y. Liu, Y. Zou, N. Gao, Z. J. Zhang, Y. G. Li, Q. B. Wang, S. Z. Li and J. Jiang, *J. Am. Chem. Soc.*, 2014, **136**, 15684.
27 T. Liu, S. X. Shi, C. Liang, S. D. Shen, L. Cheng, C. Wang, X. J. Song, S. Goel, T. E. Barnhart, W. B. Cai and Z. Liu, *ACS Nano*, 2015, **9**, 950.
28 P. Huang, J. Lin, W. W. Li, P. F. Rong, Z. Wang, S. J. Wang, X. P. Wang, X. L. Sun, M. Aronova, G. Niu, R. D. Leapman, Z. H. Nie and X. Y. Chen, *Angew. Chem., Int. Ed.*, 2013, **52**, 13958.
29 J. B. Song, X. Y. Yang, O. Jacobson, L. S. Lin, P. Huang, G. Niu, Q. J. Ma and X. Y. Chen, *ACS Nano*, 2015, **9**, 9199.
30 X. L. Liang, Y. Y. Li, X. D. Li, L. J. Jing, Z. J. Deng, X. L. Yue, C. H. Li and Z. F. Dai, *Adv. Funct. Mater.*, 2015, **25**, 1451.
31 L. H. Wang and D. Pile, *Nat. Photonics*, 2011, **5**, 183.
32 W. Feng, X. J. Zhou, W. Nie, L. Chen, K. X. Qiu, Y. Z. Zhang and C. L. He, *ACS Appl. Mater. Interfaces*, 2015, **7**, 4354.
33 Y. H. Wang, H. G. Wang, D. P. Liu, S. Y. Song, X. Wang and H. J. Zhang, *Biomaterials*, 2013, **34**, 7715.
34 R. Chen, X. Wang, X. K. Yao, X. C. Zheng, J. Wang and X. Q. Jiang, *Biomaterials*, 2013, **34**, 8314.
35 I. B. C. Matheson, J. Lee, B. S. Yamanashi and M. L. Wolbarsht, *J. Am. Chem. Soc.*, 1974, **96**, 3343.
36 H. F. Cheng, T. Kamegawa, K. Mori and H. Yamashita, *Angew. Chem., Int. Ed.*, 2014, **53**, 2910.
37 L. D. Matteis, S. G. Mitchell and J. M. Fuente, *J. Mater. Chem. B*, 2014, **2**, 7114; P. Magesan, S. Sanuja and M. J. Umapathy, *RSC Adv.*, 2015, **5**, 42506.
38 Q. Tian, F. Jiang, R. Zou, Q. Liu, Z. Chen, M. Zhu, S. Yang, J. Wang and J. Hu, *ACS Nano*, 2011, **5**, 9761.
39 G. Song, J. Shen, F. Jiang, R. Hu, W. Li, L. An, R. Zou, Z. Chen, Z. Qin and J. Hu, *ACS Appl. Mater. Interfaces*, 2014, **6**, 3915.
40 M. M. Y. A. Alsaif, K. Latham, M. R. Field, D. D. Yao, N. V. Medehkar, G. A. Beane, R. B. Kaner, S. P. Russo, J. Z. Ou and K. Kalantar-zadeh, *Adv. Mater.*, 2014, **26**, 3931.
41 L. Chen, S. Yamane, J. Mizukado, Y. Suzuki, S. Kutsuna, T. Uchimaru and H. Suda, *Chem. Phys. Lett.*, 2015, **624**, 87.

42 M. Chen, S. Tang, Z. Guo, X. Wang, S. Mo, X. Huang, G. Liu and N. Zheng, *Adv. Mater.*, 2014, **26**, 8210.
43 C. S. Guo, H. Yu, B. Feng, W. Gao, M. Yan, Z. Zhang, Y. Li and S. Liu, *Biomaterials*, 2015, **52**, 407.
44 E. S. Shibu, M. Hamada, N. Murase and V. Biju, *J. Photochem. Photobiol., C*, 2013, **15**, 53.
45 H. Arami, A. Khandhar, D. Liggitt and K. M. Krishnan, *Chem. Soc. Rev.*, 2015, **44**, 8576.